Probabilistic Feasibility Design of a Laser Powder Bed Fusion Process Using Integrated First-Order Reliability and Monte Carlo Methods

Lingbin Meng
Department of Mechanical and Energy Engineering,
Indiana University-Purdue University Indianapolis,
Indianapolis, IN 46202
e-mail: meng4@iu.edu

Xiaoping Du
Department of Mechanical and Energy Engineering,
Indiana University-Purdue University Indianapolis,
Indianapolis, IN 46202
e-mail: duxi@iu.edu

Brandon McWilliams
CCDC Army Research Laboratory,
Aberdeen Proving Ground, MD 21005
e-mail: brandon.a.mcwilliams.civ@mail.mil

Jing Zhang[1]
Department of Mechanical and Energy Engineering,
Indiana University-Purdue University Indianapolis,
Indianapolis, IN 46202
e-mail: jz29@iupui.edu

Quality inconsistency due to uncertainty hinders the extensive applications of a laser powder bed fusion (L-PBF) additive manufacturing process. To address this issue, this study proposes a new and efficient probabilistic method for the reliability analysis and design of the L-PBF process. The method determines a feasible region of the design space for given design requirements at specified reliability levels. If a design point falls into the feasible region, the design requirement will be satisfied with a probability higher or equal to the specified reliability. Since the problem involves the inverse reliability analysis that requires calling the direct reliability analysis repeatedly, directly using Monte Carlo simulation (MCS) is computationally intractable, especially for a high reliability requirement. In this work, a new algorithm is developed to combine MCS and the first-order reliability method (FORM). The algorithm finds the initial feasible region quickly by FORM and then updates it with higher accuracy by MCS. The method is applied to several case studies, where the normalized enthalpy criterion is used as a design requirement. The feasible regions of the normalized enthalpy criterion are obtained as contours with respect to the laser power and laser scan speed at different reliability levels, accounting for uncertainty in seven processing and material parameters. The results show that the proposed method dramatically alleviates the computational cost while maintaining high accuracy. This work provides a guidance for the process design with required reliability.
[DOI: 10.1115/1.4050544]

Keywords: additive manufacturing, probabilistic process design, reliability, uncertainty quantification, design for manufacturing, modeling and simulation

1 Introduction

Additive manufacturing (AM) is a group of layer-upon-layer fabrication processes based on computer-aided design models [1]. AM has become a popular fabrication method of metal components due to its capability of producing parts with complex geometries. Among the processes of metal components, laser powder bed fusion (L-PBF) is a popular AM technique that uses a high-energy laser to selectively melt or sinter a metallic powder bed. For each layer in a typical L-PBF process, a recoating blade first pushes a layer of fresh powder from the powder tank to the top of the previously built surface or the substrate. Then, a laser beam passes through a system of lenses and is reflected by a mirror that controls the laser beam spot moving along the designed path. This process is repeated in a layer-by-layer manner [2].

A major challenge in the current L-PBF field is the process variability and quality inconsistency. This is primarily due to the physical complexity involved in the laser melting process and the uncertainty involved in the processing parameters and material properties. To resolve this issue, efforts have been made in many aspects, including parametric experimental study [3–6], *in situ* experimental monitoring [7–9], process modeling [10–15], surrogate modeling [16–18], and uncertainty quantification (UQ) [19–22]. A recent review of the latest applications of machine learning (ML) in the AM field is also available in the authors' work [23]. These efforts will be summarized in the following two paragraphs.

To date, the mechanisms of the laser melting process have been extensively studied from experiments and simulations, which provide the guidance for selecting processing parameters in the process–structure–property (P–S–P) relation chain. For example, two major causes of pores formation, keyhole mode [3] and spattering [24,25], are found to be related to the laser energy density controlled by some processing parameters, such as laser power and scan speed. With this guidance, surrogate models [16–18], usually based on ML, can then generate a process map with a clear relationship between processing parameters and target properties or performance indicators such as melt pool dimension. This capability has been demonstrated in Refs. [17,18,26]. The process map, though is helpful for process design, does not take the uncertainty of the input variables into account. The reliability remains unknown on the process map. Additionally, the Gaussian process (GP) models were employed to capture the surface changes and variation over the polishing process of 3D-printed Ti–6Al–4V alloy samples [27]. The correlation parameters associated with polishing stages revealed the subtle features of the surface as well as their changes during the polishing process [27]. In Ref. [28], a deep neural network (NN)-based ML technique was used to mitigate the scattering effect in light-based 3D printing methods. The NN was employed to study the highly sophisticated relationship between the input digital masks and their corresponding output 3D-printed structures. Furthermore, the NN was used to model an inverse 3D printing process, where it took desired printed structures as inputs and subsequently generated grayscale digital masks that

[1]Corresponding author.

Manuscript received April 1, 2020; final manuscript received March 1, 2021; published online March 29, 2021. Assoc. Editor: Qiang Huang.

optimized the light exposure dose according to the desired structures' local features [28].

Built upon this knowledge, the uncertainty, which is the main cause of process inconsistency, unpredictability, and unrepeatability, has been investigated using Monte Carlo simulation (MCS) [29] and polynomial chaos expansions [19]. The outcome of these UQ efforts is the uncertainty of the output quantity in terms of a series of input random variables. This is desirable, but insufficient for process design optimization. UQ merely provides the reliability of the current design. If the current design is rejected by the design requirements, what improvement shall be made? UQ does not answer this question. In this regard, UQ is an appropriate tool for assessment of existing designs, but not for creating new design. In other words, the link between UQ and optimal process design is still missing. Efficient tools for reliability analysis and process optimization in the L-PBF field are needed.

With the above discussions in mind, we propose a new probabilistic method that links UQ with the L-PBF process design and reliability. Instead of directly quantifying uncertainty and reliability, we specify a feasible design region for given design requirements at a specified reliability level. The feasible design region allows researchers to select process design variables in the feasible design region so that the required reliability can be ensured. It also provides constraints on design variables when optimization is used.

The structure of the paper is arranged as follows. Probabilistic design and reliability analysis methods are reviewed in Sec. 2. Then the proposed new method using the combined first-order reliability method (FORM) and MCS is presented in Sec. 3, followed by a case study in Sec. 4, where a criterion based on normalized enthalpy [3,30] is used to identify the conduction mode in the L-PBF process. The feasible design regions are determined by the given reliability levels. Section 5 provides conclusions and suggested future work.

2 Review of Probabilistic Design and Reliability Analysis

This work focuses on the probabilistic process design of the L-PBF process and is based on FORM and MCS. These methods are briefly reviewed here. The normalized enthalpy criterion is also discussed, since it is the design requirement in the case study for the L-PBF design.

2.1 Probabilistic Design. In an L-PBF process, the design and manufacture of a component are subject to one or multiple requirements, such as strength, geometric accuracy, and other desired properties. These quantities (output) corresponding to the requirements are determined by design variables (input), such as the laser power and scan speed. Since uncertainty exists in the input variables, the requirements may not always be satisfied. If the probability of satisfying a design requirement is denoted by reliability, the reliability may not be always 100% or 1.0. A typical probabilistic process design identifies the design variables so that the reliability is equal to or higher than the target reliability [31–33].

Probabilistic design uses limit-state functions. A limit-state function specifies the functional relationship between an output variable Y and input variables $\mathbf{X}$ and is given by [34]

$$Y = g(\mathbf{X}) \tag{1}$$

here Y is the output quantity of interest, and $\mathbf{X} = (X_1, X_2, \ldots, X_n)$ is a vector of input variable with n being the size of $\mathbf{X}$. When uncertainty is associated with the input variables, they are modeled as random variables with their probability density function (PDF) $f_{X_i}(x_i)$, $i = 1, \ldots, n$. In this study, we assume that the input random variables are independent. Without losing generality, we assume that a design requirement is satisfied if $Y = g(\mathbf{X}) > 0$; in other words, a failure occurs if $Y = g(\mathbf{X}) \leq 0$. The reliability R is then given by

$$R = \Pr\{g(\mathbf{X}) > 0\} \tag{2}$$

where $\Pr\{\cdot\}$ denotes a probability.

For the L-PBF process, Y can be one of the properties of the printed parts, as well as some quality indicator such as the melt pool dimension. $\mathbf{X}$ usually includes processing parameters, such as laser power, laser scan speed, laser beam size, and layer thickness, as well as powder properties, including absorption coefficient, powder size distribution, and thermal conductivity.

A limit-state function is usually derived from physical principles, and it may be a black-box model. It may also be obtained from experiments. If the limit-state function, such as a finite element analysis model, is computationally expensive, its surrogate can be constructed. The computational cost of a surrogate model is low, typically in seconds or minutes. For a high dimensional and highly nonlinear limit-state function, the surrogate model can be built by ML methods [16–18].

2.2 Uncertainty Quantification and Reliability Analysis. During the probabilistic design, the reliability in Eq. (2) should be calculated, and this is the task of reliability analysis, whose objective is to find R given PDFs $f_{X_i}(x_i)$, $i = 1, \ldots, n$ and $g(\mathbf{X})$. Data acquisition is essential to construct a limit-state function $g(\mathbf{X})$ and estimate PDFs $f_{X_i}(x_i)$, $i = 1, \ldots, n$. Conventional way for data acquisition is to use experimental measurements, and this may be time consuming and costly. A more actionable way is by means of computational models after experimental validation, in order to alleviate the need of the expensive experiments. It should be noted that experimental measurements will introduce aleatory (random) uncertainty whereas computational models will have their model uncertainty [21]. The uncertainty sources and data acquisition are briefly discussed below and will also be elaborated further for the case studies in Sec. 4.1.

The sources of uncertainty involved in the L-PBF process have been summarized in Ref. [21]. They can be classified into two categories: (1) aleatory uncertainty, which refers to the irreducible natural variability, and (2) epistemic uncertainty, which refers to the reducible uncertainty due to lack of knowledge of parameters, as well as approximations and assumptions introduced during the modeling process. The epistemic uncertainty can be further classified into two subgroups: (1) data uncertainty due to the imprecise measurements and (2) model uncertainty due to the assumptions, simplifications, and numerical discretizations involved in the model [21].

An example is the aleatory uncertainty and the data uncertainty in the laser power and scan speed, which strongly affect the input energy density and the melt pool dynamics, due to the variation of the laser 3D printer. Another example is the imprecise measurements (data uncertainty) of the material properties, such as the absorption coefficient to the laser energy and thermal diffusivity. There are many uncertainty and reliability analysis methods, and two of them are reviewed in Secs. 2.3 and 2.4.

2.3 Monte Carlo Simulation. MCS [19–21,29,35] is a numerical algorithm that relies on repeated random sampling. N samples of $\mathbf{X}$ are first generated from the distributions of $\mathbf{X}$, and then the limit-state function is evaluated at the samples of $\mathbf{X}$, resulting in samples of Y. The number of failures n_f is obtained by counting the number of samples of Y in the failure region $Y<0$. The probability of failure is estimated by

$$p_f = \frac{n_f}{N} \tag{3}$$

and the reliability is given by $R = 1 - p_f$. The advantage of MCS is that it is easy to use and its accuracy does not depend on the number of input random variables and their variation. Its computational cost, however, will be significant with a small probability of failure. For instance, if $p_f = 10^{-6}$, for sufficient accuracy approximately 10^8 samples are needed, and this means that the limit-state function has to be called 10^8 times.

2.4 First-Order Reliability Method. FORM is one of the most commonly used reliability methods [34]. It predicts the reliability $R = \Pr\{g(\mathbf{X}) > 0\}$, given the limit-state function and distributions of $\mathbf{X}$. In this work, we use the inverse FORM [36]. It solves an inverse problem: find the limit state $g(\mathbf{X}) = c$, given the limit-state function, distributions of $\mathbf{X}$, and reliability R, so that

$$\Pr\{g(\mathbf{X}) > c\} = R \tag{4}$$

The first step is to transform the random variables X_i $(i = 1, \ldots, n)$ into standard normal variables U_i by

$$F_{X_i}(X_i) = \Phi(U_i) \tag{5}$$

where $F_{X_i}(X_i)$ is the cumulative density function (CDF) of X_i, and $\Phi(U_i)$ is the CDF of U_i. The transformation from the X-space to the U-space is denoted by $\mathbf{X} = T(\mathbf{U})$. We then have the limit-state function in the U-space as follows:

$$Y = g(\mathbf{X}) = g(T(\mathbf{U})) \tag{6}$$

The joint probability density of $\mathbf{U}$ is symmetric with its peak point at the origin of the U-space since all the elements $\mathbf{U}$ follow standard normal distributions whose peaks are at the origin. The close is a realization of $\mathbf{U}$, the higher is the probability density. The key idea is to find the most probable point (MPP). The MPP is named due to it has the highest probability density at the limit state $g(T(\mathbf{U})) = c$. As a result, the MPP is the shortest distance point from the origin to the surface $g(T(\mathbf{U})) = c$. The limit-state function is then linearized at the MPP, which minimizes the accuracy loss due to the linearization.

The MPP $\mathbf{u}^*$ is found by solving the following optimization problem:

$$\begin{cases} \min\limits_{\mathbf{u}} g(T(\mathbf{U})) \\ \text{subject to } \|\mathbf{u}\| = \beta \end{cases} \tag{7}$$

where $\|\cdot\|$ denotes the magnitude of a vector, and β is the reliability index, given by

$$\Phi(\beta) = R \tag{8}$$

The limit state is then found by

$$c = g(T(\mathbf{u}^*)) \tag{9}$$

Since $\mathbf{u}^*$ is the shortest distance point to the surface or contour $g(T(\mathbf{U})) = c$, $\mathbf{u}^*$ is perpendicular to $g(T(\mathbf{U})) = c$. The direction of $\mathbf{u}^*$ is towards the failure region or the direction along which the limit-state function decreases. Note that the gradient $g(T(\mathbf{U}))$ is in the direction along which the limit-state function increases and is perpendicular to the contour of the limit-state function. Then $\mathbf{u}^*$ is in the opposite direction of the gradient of $g(T(\mathbf{U}))$ at $\mathbf{u}^*$, where $\nabla g(T(\mathbf{U})) = (\partial g/\partial U_1, \ldots, \partial g/\partial U_n)|_{\mathbf{u}^*}$. This gives

$$\frac{\mathbf{u}^*}{\beta} = -\frac{\nabla g(T(\mathbf{U}))}{\|\nabla g(T(\mathbf{U}))\|} = -\alpha(\mathbf{u}^*) \tag{10}$$

where

$$\alpha(\mathbf{u}^*) = \frac{\nabla g(T(\mathbf{U}))}{\|\nabla g(T(\mathbf{U}))\|} \tag{11}$$

which is a unit vector along the gradient direction.

The goal of FORM now becomes searching for the MPP point $\mathbf{u}^*$. According to Eq. (10), the MPP point $\mathbf{u}^*$ satisfies

$$\mathbf{u}^* = -\beta\alpha(\mathbf{u}^*) \tag{12}$$

The MPP search process is iterative, and the search algorithm includes the Hasofer–Lind and Rackwitz–Fiessler algorithm [34,37]. For the work in this study, since β is known, for the ith iteration, we have

$$\mathbf{u}_i = -\beta\alpha(\mathbf{u}_{i-1}) \tag{13}$$

2.5 Normalized Enthalpy Criterion. To use probabilistic analysis and design, we need to create limit-state functions. We now discuss the construction of limit-state functions for the L-PBF process. We take the normalized enthalpy criterion as an example, which was proposed by Hann et al. [30] and quantified by King et al. [3] for keyhole mode identification for 316L stainless steel. The criterion was later applied in a GP-based ML model in Ref. [17] to predict the remelted depth of single tracks, as a function of combined laser power and laser scan speed in a L-PBF process.

The criterion of the occurrence of the keyhole mode is

$$\frac{\Delta H}{h_s} = \frac{AP}{\rho h_s \sqrt{\pi D v (r/2)^3}} \geq 30 \tag{14}$$

where ΔH is the specific enthalpy, h_s is the enthalpy at melting, A is the material absorption coefficient to the laser power, P is the laser power, ρ is the density, D is the thermal diffusivity, v is the laser scan speed, and r is the laser beam radius. For example, with increased laser power P, decreased laser scan speed v, increased absorption coefficient, or decreased laser beam radius (which make the laser more focused), the laser energy density will increase, and so does the quantity $\Delta H/h_s$ based on the criterion. This satisfies the fact that the keyhole mode occurs when the laser energy density is too high. The preferred conduction mode region is $\Delta H/h_s < 30$.

The limit-state function according to the criterion is constructed by

$$Y = g(\mathbf{X}) = g(A, P, \rho, h_s, D, v, r) = 30 - \frac{AP}{\rho h_s \sqrt{\pi D v (r/2)^3}} \tag{15}$$

where $\mathbf{X} = (A, P, \rho, h_s, D, v, r)$. If $Y > 0$, we would have the preferred conduction mode region, and if $Y \leq 0$, we would get a failure if we consider the keyhole mode as a failure. Note that in reality a state in keyhole mode may not be necessarily a failed state, but it is the state we want to avoid. If the laser scan speed v and laser power P are the two processing parameters we can control during the L-PBF process, we can plot the safe (conduction) region and failure (keyhole) region specified by the limit-state function as shown in Fig. 1.

To avoid the keyhole mode, we can select the design variables (v, P) in the safe region. The curve that divides the safe and failure regions, however, is not fixed due to the randomness in $\mathbf{X}$. To accommodate the uncertainty, we develop a probabilistic method, so that the safe region can ensure reliability equal to or higher than the target reliability.

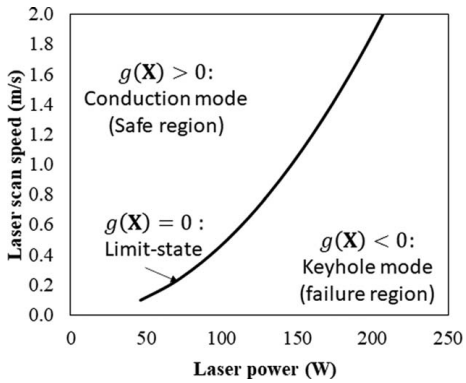

Fig. 1 Limit-state function constructed by the normalized enthalpy criterion for keyhole mode identification for L-PBF fabricated 316L stainless steel

3 A Probabilistic Method for Identifying a Feasible Design Region

The objective of this work is to identify a feasible design region for a given requirement at a desired reliability level. If a design point falls into the feasible design region, the design requirement will be satisfied with a probability that is no less than the desired reliability. Identifying the feasible design region is computationally expensive if we use MCS to do so. This is the reason in this study that we develop an efficient method to generate a feasible design region for process design while maintaining the same accuracy level as MCS.

3.1 Overview. A limit-state function $Y = g(\mathbf{X})$ is available for a design requirement $Y > 0$, and the input variables $\mathbf{X}$ are random. To satisfy the requirement $Y = g(\mathbf{X}) > 0$ at reliability $R = \Pr(g(\mathbf{X}) > 0)$, we need to change the design variables, which are a subset of $\mathbf{X}$. Let the design variables be denoted as $\mathbf{d} = (d_1, d_2, \ldots, d_m)$, which are deterministic variables, for instance, the means of some random variables in $\mathbf{X}$, with m being the number of design variables. Therefore, in Eq. (15), we could include the means of the laser scan speed, v, and laser power, P, as design variables. The other random variables, including A, ρ, h_s, D, and r, are in the set $\mathbf{X}$ but not in $\mathbf{d}$. By considering the design variables, the limit-state function is rewritten as $Y = g(\mathbf{X}; \mathbf{d})$. Since the X-to-U transformation also depends on $\mathbf{d}$ if it contains distribution parameters $\mathbf{X}$, the transformation is expressed by $\mathbf{X} = T(\mathbf{U}; \mathbf{d})$. The limit-state function in the U-space is then given by $Y = g(T(\mathbf{U}; \mathbf{d}); \mathbf{d})$. In this study, we assume that all the random variables in $\mathbf{X}$ are independent. For the general case where dependent random variables exist, they can be transformed into independent variables, and consequently, the proposed method can still be used [38]. The task is summarized as follows:

Given: The distributions of $\mathbf{X}$, limit-state function $Y = g(\cdot)$, and required reliability R.

Find: Domain of $\mathbf{d}$ such that $\Pr\{g(\mathbf{X}; \mathbf{d}) > 0\} = R$.

The domain of $\mathbf{d}$ specified above is the reliability-based feasible design region. Denote the feasible design region by $H(\mathbf{d}) = 0$. Once feasible region is available, design variables can be selected from it. We are particularly interested in plotting the region so that it is convenient to use the graph. Plotting $H(\mathbf{d}) = 0$ or $\Pr\{g(\mathbf{X}; \mathbf{d}) > 0\} = R$, however, is computationally demanding.

Take a two-dimensional problem as an example. Let $\mathbf{d} = (d_1, d_2)$, and therefore $H(d_1, d_2) = 0$, or $\Pr\{g(\mathbf{X}; d_1, d_2) > 0\} = R$. Suppose we use 100 points to plot the curve, and we then discretize the range of d_1 with 100 points. For each point of d_1, we solve for d_2 from $\Pr\{g(\mathbf{X}; d_1, d_2) > 0\} = R$. This is an inverse probabilistic analysis, meaning that given the probability R, find d_2, which may be a distribution parameter of one random variable in $\mathbf{X}$. One inverse probabilistic analysis will need a number of direct probabilistic analyses, which find the probability $\Pr\{g(\mathbf{X}; d_1, d_2) > 0\}$ for a given value of d_2. If the probability does not equal to R, d_2 will be changed. This process continues until $\Pr\{g(\mathbf{X}; d_1, d_2) > 0\} = R$. Suppose we use MCS and the required reliability is $R = 0.99999$ (the probability of failure $p_f = 10^{-5}$). Also assuming that we use a sample size of 10^7 for one direct probabilistic analysis, an inverse probabilistic analysis needs 10 direct probabilistic analyses, and solving for d_2 needs 10 function calls. Then the total number of calling the limit-state function $g(\mathbf{X}; d_1, d_2)$ will be $100 \times 10 \times 10 \times 10^7 = 10^{11}$ times. Such a high computational cost will be unaffordable for many applications.

To overcome the above-mentioned obstacles, in this study, we develop a new efficient method based on the inverse FORM. The feasible design region can be quickly generated by the proposed method with much less function calls. If a higher accuracy is needed for critical applications, the accuracy will then be checked with MCS. If the accuracy is not satisfactory, the MCS result will be used to refine the design region. The direct use of the inverse FORM will involve a double-loop procedure, as illustrated in Table 1 in Sec. 3.2. The outer loop is to search for the MPP $\mathbf{u}^*$ for a given set of $\mathbf{d}$, and the inner loop is solved for $\mathbf{d}$ from $H(\mathbf{d}) = g(T(\mathbf{u}^*; \mathbf{d}); \mathbf{d}) = 0$. To further improve the efficiency, we propose to combine the two loops so that solving $H(\mathbf{d}) = g(T(\mathbf{u}^*; \mathbf{d}); \mathbf{d}) = 0$ is embedded in the MPP search algorithm.

Table 1 FORM-based feasible design

Procedure: FORM-based feasible design
Input
  Required reliability R
  CDFs $F_{X_i}(\cdot)$, $i = 1, 2, \ldots, n$
  Initial design point $\mathbf{d}_0$
  Initial MPP $\mathbf{u}_0$
  Convergence tolerance δ
Output: $\mathbf{d}$
$\mathbf{u} = \mathbf{u}_0$
$\mathbf{d} = \mathbf{d}_0$
$\beta = \Phi^{-1}(R)$
convergence = *false*
while *convergence* = *false*
  $\mathbf{u}_{\text{old}} = \mathbf{u}$
  $\mathbf{x} = T^{-1}(\mathbf{u}; \mathbf{d})$
  $\dfrac{\partial g}{\partial u_i} = \dfrac{\partial g}{\partial X_j}\dfrac{dx_i}{\partial u_i}$
  $\nabla g = \left(\dfrac{\partial g}{\partial u_i}\right)_{i=1,n}$
  $\alpha = \dfrac{\nabla g}{\|\nabla g\|}$
  $\mathbf{u} = \beta\alpha$
  $\mathbf{d}$ = solution to $g(T(\mathbf{u}; \mathbf{d}); \mathbf{d}) = 0$
  $\varepsilon = \|\mathbf{u} - \mathbf{u}_{\text{old}}\|$
  if $\varepsilon < \delta$ **then**
    convergence = *true*
  end if
end while

3.2 First-Order Reliability Method for Generating a Feasible Design Region. As discussed above, design variables are solved from $H(\mathbf{d}) = g(T(\mathbf{u}^*; \mathbf{d}); \mathbf{d}) = 0$ where $\mathbf{u}^* = \beta\alpha(\mathbf{u}^*)$ is indicated in Eq. (12). Equation (11) gives

$$\alpha(\mathbf{u}^*) = \frac{\nabla g(T(\mathbf{U}; \mathbf{d}); \mathbf{d})}{\|\nabla g(T(\mathbf{U}; \mathbf{d}); \mathbf{d})\|} \tag{16}$$

Function $H(\mathbf{d})$ becomes

$$H(\mathbf{d}) = g\left(T\left(\beta \frac{\nabla g(T(\mathbf{U}; \mathbf{d}); \mathbf{d})}{\|\nabla g(T(\mathbf{U}; \mathbf{d}); \mathbf{d})\|}; \mathbf{d}\right); \mathbf{d}\right) = 0 \tag{17}$$

Solving Eq. (17) requires an iterative procedure. The first step is to find the reliability index by [34]

$$\beta = \Phi^{-1}(R) \tag{18}$$

where the required reliability R is greater than 0.5.

Suppose at iteration i, the design variables are obtained from the previous or the $(i-1)$th iteration, and the MPP is $\mathbf{u}$ in the U-space. We convert them into the original random variables in the X-space by $\mathbf{x} = T^{-1}(\mathbf{u})$, where the transformation $T^{-1}(\cdot)$ is given in Eq. (5). We calculate the derivative of the limit-state function at and obtain $\partial g/\partial X_j$, where $j = 1, 2, \ldots, n$. The derivative of the limit-state function at $\mathbf{u}$ is then

$$\frac{\partial g}{\partial u_j} = \frac{\partial g}{\partial X_j}\frac{dx_j}{\partial u_j} \tag{19}$$

where $dx_j/\partial u_j$ can be derived from Eq. (5).

$$\frac{dx_j}{\partial u_j} = \frac{\phi(u_j)}{f_{X_j}(x_j)} \tag{20}$$

where $\phi(\cdot)$ and $f_{X_j}(\cdot)$ are the PDF of U_j and X_j, respectively. Then the gradient is $\nabla g(T(\mathbf{u}^i; \mathbf{d}); \mathbf{d}) = (\partial g/\partial U_1, \ldots, \partial g/\partial U_n)|_{\mathbf{u}}$, and the associated unit vector is $\alpha(\mathbf{u}) = (\nabla g(T(\mathbf{u}^i; \mathbf{d}); \mathbf{d}))/(\|\nabla g(T(\mathbf{u}^i; \mathbf{d}); \mathbf{d})\|)$.

Then the MPP is updated to

$$\mathbf{u} = \beta\alpha(\mathbf{u}) \tag{21}$$

Once the $\mathbf{u}$ is updated, we solve $H(\mathbf{d}) = g(T(\mathbf{u}^*; \mathbf{d}); \mathbf{d}) = 0$ and obtain a new set of design variables $\mathbf{d}$. Thus, one iteration is complete. Then convergence is checked. If the distance between the new MPP on the left-hand side of Eq. (19) is sufficiently close to the previous MPP on the right-hand side of the equation, the MPP is found; otherwise, we calculate the gradient of the limit-state function at the updated MPP and then find a new MPP. We repeat this process until convergence criterion is met. Once the iterative process is complete, we obtain a design point $\mathbf{d}$ for the feasible design region. By repeating this iterative process multiple times, we obtain a number of design points, which will then result in a boundary of the feasible design region.

The convergence is judged by

$$\varepsilon = \|\mathbf{u}_{\text{new}} - \mathbf{u}_{\text{old}}\| \tag{22}$$

where $\mathbf{u}_{\text{new}}$ and $\mathbf{u}_{\text{old}}$ are the MPPs at the current iteration and previous iteration, respectively. The convergence criterion is: given a tolerance δ, we will terminate the search if $\varepsilon < \delta$. δ can be set to 0.01 or 0.001.

The procedure of the FORM-based feasible design for solving one design point is summarized in Table 1.

If we use the above algorithm to produce a sufficient number of design points, we can then generate a feasible design region. The algorithm requires evaluating the gradient of the limit-state function and solving the equation given by $g(T(\mathbf{u}; \mathbf{d}); \mathbf{d}) = 0$. It does not involve any random sampling and is therefore computationally efficient. Since the method employs the most commonly used FORM, its accuracy should be acceptable for most applications. The accuracy, however, may deteriorate if the limit-state function is highly nonlinear around the MPP in the U-space.

There are two possible ways to improve the accuracy. The first way is to use MCS based on the result from the proposed method, while the second way is to use the second-order reliability method, which also uses the second derivatives of the limit-state function. In this study, we choose the former method for efficiency.

3.3 Accuracy Improvement by Monte Carlo Simulation.

The strategy is to use MCS to accurately calculate the reliability at the design point $\mathbf{d}$, which is obtained from the above FORM-based feasibility design. Denote the reliability from MCS by R_{MCS}, and let the difference from the required reliability be $\varepsilon_R = R_{\text{MCS}} - R_{\text{Req}}$. If $|\varepsilon_R|$ is greater than a tolerance δ_R, we will adjust the required reliability by

$$R_n = \frac{R_{n-1}R_{\text{Req}}}{R_{\text{MCS}}} \tag{23}$$

where R_n denotes the input reliability of FORM at the nth iteration. Then the algorithm in Table 1 is called. To reduce the computational cost, we use the design point $\mathbf{d}$ and MPP $\mathbf{u}$ from the last feasibility design as the initial design point and MPP, respectively. This process is repeated until the convergence criterion is met, and convergence can be reached with a few iterations. As a result, no inverse MCS is needed, and the number of direct MCS is minimized. The tolerance δ_R is determined by the accuracy requirement for a specific application. In this work, we employ a relative tolerance, such that

Table 2 Integrated FORM and MCS

Procedure: FORM/MCS-based feasible design
Input
  Required reliability R_{Req}
  CDFs $F_{X_i}(\cdot)$, $i = 1, 2, \ldots, n$
  Initial design point $\mathbf{d}_0$
  Initial MPP $\mathbf{u}_0$
  Convergence tolerance δ for FORM
  Convergence tolerance δ_R for reliability
Output: $\mathbf{d}$
convergence = *false*
while *convergence* = *false*
  $\mathbf{u} = \mathbf{u}_0$
  $\mathbf{d} = \mathbf{d}_0$
  $\beta = \Phi^{-1}(R)$
  Call FORM-based feasibility design (see Table 1)
  Obtain $\mathbf{d}$, $\mathbf{u}$
  Call MCS
  Obtain R_{MCS}
  $\varepsilon_R = R_{\text{MCS}} - R_{\text{Req}}$
  if $|\varepsilon_R| < \delta_R$ **then**
  convergence = *true*
  end if
  $R = \frac{RR_{\text{Req}}}{R_{\text{MCS}}}$
  $\mathbf{u}_0 = \mathbf{u}$
  $\mathbf{d}_0 = \mathbf{d}$
end while

$$\delta_R = cp_r \tag{24}$$

where c is a relative coefficient. For example, we set $c = 0.5$. If $R_{\text{Req}} = 0.99999$, then $p_r = 10^{-5}$ and $\delta_R = 5 \times 10^{-6}$. Therefore, upon convergence, the actual reliability will be 0.99999 ± 0.000005. The algorithm of the d FORM and MCS is provided in Table 2.

4 Case Studies

In this section, the proposed method is demonstrated by its application for the reliability-based L-PBF process design.

4.1 Case 1: Normal Distribution and Standard Deviations are Fractions of Their Means

4.1.1 Limit-State Function and Model Input. In this case, standard deviations change with respect to the means and are fractions of their means. The limit-state function for the normalized enthalpy criterion is given in Eq. (15). There are seven random input variables, and three of which are design variables, including the laser power P, laser scan speed v, and laser beam radius r. During the process design, the means of the three random variables are to be changed. In this study, we assume that the mean of the laser beam radius r is fixed due to its low flexibility. Then the design problem becomes two-dimensional, and the design variables are the means μ_P and μ_v of P and v, respectively, or their nominal values, namely, $\mathbf{d} = (\mu_P, \mu_v)$. Note that the reliability analysis is seven-dimensional because seven random variables are involved.

We identify the feasible design region for the means $\mathbf{d} = (\mu_P, \mu_v)$. Since we need to plot a two-dimensional curve for the feasible design region, we discretize one variable and solve for the other at the discretized points of the first one. We divide the nominal values of v, or μ_v, into 0.1, 0.2, …, 2.0 m/s and then solve for the corresponding nominal values of P, or μ_P. Since there are in total 20 points, we call the algorithm in Table 2 20 times, searching for a set of μ_P for a given set of μ_v, namely, 0.1, 0.2, …, 2.0 m/s. For the stop criteria, we use $c = 0.5$ in Eq. (15) and $\delta = 0.01$ in Eq. (13).

We need to know the distributions of all the seven input random variables. For this case study, we use the distributions from previous research and experiments reported in the literature. Table 3

Table 3 Distributions of input random variables

	Unit	Mean, μ	Standard deviation, σ	Distribution	References
P	W	μ_P	$0.025\mu_P$	Normal	[19,22,39]
v	m/s	μ_v	$0.015\mu_v$	Normal	[19,22,39]
A	–	0.4	$0.2\mu_A$	Normal	[3,40,41]
ρ	kg/m^3	7980	$0.01\mu_\rho$	Normal	[17,29,39]
D	m^2/s	5.38×10^6	$0.1\mu_D$	Normal	[17,22]
r	m	2.70×10^{-5}	$0.04\mu_r$	Normal	[19]
h_s	J/kg	1.20×10^6	$0.1\mu_{h_s}$	Normal	[17,42]

summarizes the distributions with the associated references. All the seven random variables follow normal distributions, and their standard deviations are fractions of their means. For specific applications, the distributions will be different, and the effect of distribution types is analyzed in Secs. 4.2 and 4.3.

4.1.2 Reliability-Based Feasibility Design. We first generate a feasible design region for an allowable probability of failure of $p_f = 10^{-6}$ or a target reliability of $R = 0.999999$. The feasible design region obtained from FORM, with the dotted line, is shown in Fig. 2, where the region above the curve is the feasible design region for the L-PBF process. If a design point (μ_P, μ_v) is chosen above the curve, the probability in the keyhole mode will be less than 10^{-6}. If the design point is on the curve, the probability in the keyhole mode will be 10^{-6}.

For comparison, we also plot the deterministic feasible design region generated using the means of all the seven random input variables. If the design point is on the curve of the deterministic feasible design, the probability of the occurrence of keyhole mode will be very high, around 0.5. The deterministic feasible design region occupies most of the entire design space while the reliability feasible design region is reduced significantly, suggesting that the effect of uncertainty is significant.

The proposed method with FORM is extremely efficient. The computational time for the entire curve is only 0.07 s with an Intel Core i7-8750H processor and 32 GB RAM. If higher accuracy is preferred, the FORM/MCS method can be formed. It runs MCS after the feasible design region is found by FORM. Figure 2 shows that the curve from the FORM/MCS method with a sample size of 10^9 is very close to the one from FORM, and this indicates that FORM is not only efficient but also accurate. The computational cost of the FORM/MCS method is 43,209 s, much higher than that of FORM. If direct MCS is used, the computational cost is 371,085 s, and this indicates that the proposed FORM and FORM/MCS methods can cut the computational cost significantly.

Different applications may require different reliability targets. We also perform the proposed method for other levels of required reliability, and the associated probabilities of failure are 10^{-2}, 10^{-3}, 10^{-4}, and 10^{-5}, respectively. The reliability feasible design regions from FORM/MCS are plotted in Fig. 3.

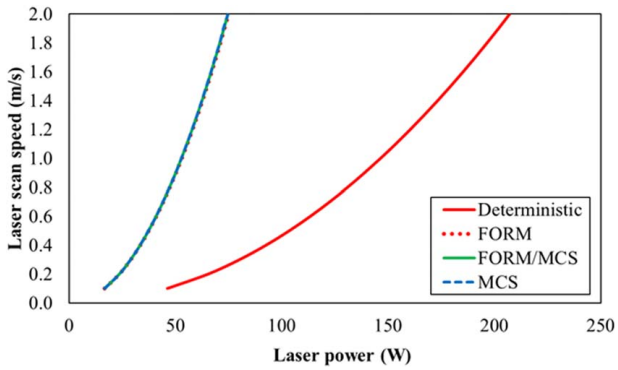

Fig. 2 Reliability contours at $p_f = 10^{-6}$ from FORM, FORM/MCS, MCS, and deterministic methods in case 1

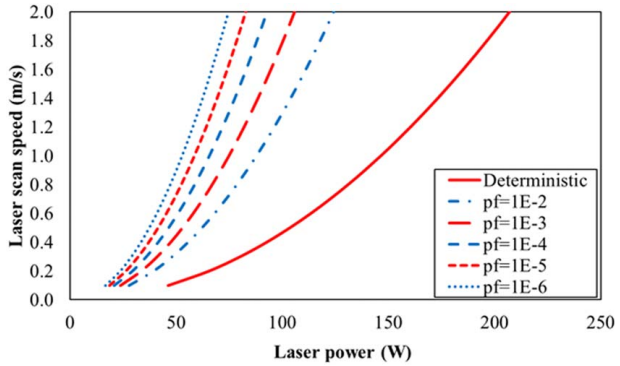

Fig. 3 Reliability feasible design regions for different probabilities of failure (pf) in case 1

Table 4 Comparison of computational costs among FORM, FORM/MCS, and MCS methods

Method	$p_f = 10^{-2}$	$p_f = 10^{-3}$	$p_f = 10^{-4}$	$p_f = 10^{-5}$	$p_f = 10^{-6}$
FORM	0.07 s	0.07 s	0.07 s	0.07 s	0.07 s
FORM/MCS	5 s	47 s	440 s	4351 s	43,209 s
MCS	41 s	387 s	3786 s	37,249 s	371,085 s

Figure 3 also demonstrates that the boundaries of the reliability feasible design region are nonlinear and are increasing functions. It also shows that the increasing reliability reduces the feasible design region, or the boundaries shift to left of the figure. In other words, higher reliability results in a narrower design space.

The computational costs for different reliability targets are summarized in Table 4. It is clear that the cost of FORM/MCS or the direct MCS increases when the required reliability increases, since the number of Monte Carlo samples needed for higher reliability is larger for sufficient accuracy. The cost of FORM remains almost constant, not affected by the required reliability. Overall, FORM shows its excellent efficiency and good accuracy. If the FORM/MCS method is unaffordable, the reliability feasible design region can be used; to meet the required reliability with high accuracy, a design point can be selected no close to the boundary of the reliability feasible design region.

4.2 Case 2: Normal Distribution and Constant Standard Deviations. In case 1, the standard deviations change with respect to the means. In some L-PBF processes, however, the standard deviations are constant for certain parameters, such as the uncertainty due to imprecise measurements of laser power and scan speed. To evaluate the proposed method, we study one case with fixed standard deviations, $\sigma_P = 1$ W and $\sigma_v = 0.1$ m/s. The other distributions remain unchanged. The permitted probability of failure is still 10^{-6}.

The reliability feasible design regions of case 2 from FORM and FORM/MCS are plotted in Fig. 4. Similar to case 1, Fig. 4 shows that the curve from FORM is still very close to the one from FORM/MCS, which indicates the high accuracy of FORM in this scenario. The computational cost of FORM is still 0.07 s, indicating its high efficiency.

4.3 Case 3: Non-Normal Distribution. Only normal distributions are involved in the above two cases. In practice, non-normal distributions may also exist. The proposed method can also be

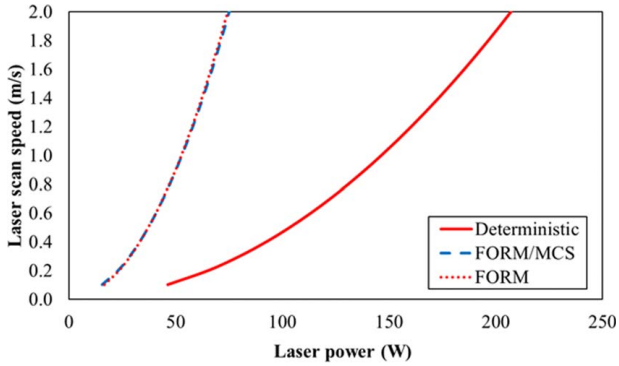

Fig. 4 Reliability contours at $p_f = 10^{-6}$ from FORM, FORM/MCS, and deterministic methods in case 2

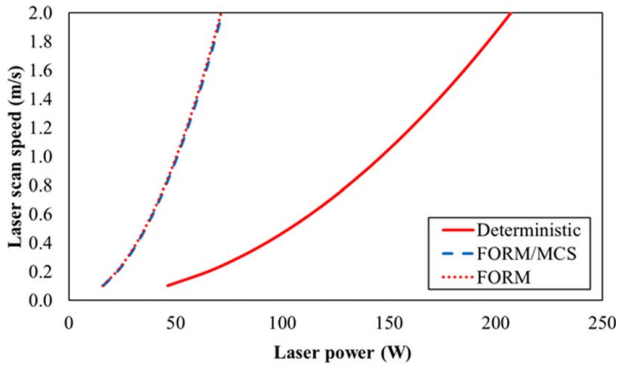

Fig. 5 Reliability contours at $p_f = 10^{-6}$ from FORM, FORM/MCS, and deterministic methods in case 3

used for any continuous unimodal distributions and works well with non-normal distributions including lognormal, Gumbel, Weibull, extreme value, and gamma distributions [34]. For L-PBF, uniform distribution is a common type of uncertainty, whereas other non-normal distribution types have not been reported in the literature. Therefore, we study a case where the laser scan speed follows a uniform distribution, as reported in Ref. [19]. The lower and upper bounds of the uniform distribution are $0.97\mu_v$ and $1.03\mu_v$, respectively, where μ_v is given in Table 3. The permitted probability of failure is still 10^{-6}. The other distributions remain the same as case 1.

Figure 5 displays the reliability feasible design regions of case 3 from FORM and FORM/MCS at $p_f = 10^{-6}$. As mentioned in Sec. 2.4, the transformation from non-normal distribution to normal distribution in FORM is nonlinear, and therefore an error is expected to occur in case 3. However, as shown in Fig. 5, the curve from FORM still matches very well with the one from FORM/MCS. This verifies the outstanding accuracy and flexibility of FORM.

Case 2 and case 3 demonstrate the flexibility of the proposed method. The reliability feasibility regions in the three cases are different, showing the impact of distribution types and distribution parameters. The three cases also indicate the high accuracy and efficiency of the proposed FORM-based method.

Note that the model we use is explicit. But we actually treat the model as a black box. The model is coded as a separate function. During the iterative process of building the feasible region, the FORM/MCS algorithm generates an input, calls the model, and receives the model output. The model is a black box to the calling algorithm. If the model we use was a black-box numerical simulation model, the process would be the same. The proposed algorithm is therefore applicable to both explicit and implicit models.

5 Conclusions and Future Work

Uncertainty exists in all aspects of AM, including its process design. If the uncertainty is significant, it is imperative to account for uncertainty to ensure that the reliability and quality requirements are satisfied. This work develops a reliability-based feasibility design to identify a feasible design region for selecting design variables for L-PBF AM process design. The major conclusions from this study are summarized as follows:

(1) The input of the proposed method includes the following:
- The limit-state function for a given requirement. It can be an explicit model or a black-box model.
- Distributions of input random variables.
- Design variables, which are the means of process design variables (part of the input random variables).
- The target reliability.

(2) The output of the proposed method is a feasible design region.

(3) If a design point is selected from the feasible design region, the probability of satisfying the requirement is no less than the target reliability.

(4) The proposed method is based on the FORM and MCS. For higher efficiency, only FORM can be performed when the computational cost of calling the limit-state function is high. Both the FORM and FORM/MCS are much efficient than the direct MCS.

(5) The three case studies in L-PBF process demonstrate that the impact of uncertainty on the process design is significant, since the feasible design region is reduced significantly, especially when high reliability is required. The results show that the required reliability of 99.9999% can narrow the design space more than half.

(6) The proposed method is not limited to AM. It can be used to generate reliability feasible design regions for other applications if the input indicated in (1) is available.

For the future work, the efficiency can be further enhanced for computationally expensive limit-state functions, especially for those from multiphysics and multiscale simulations. The future work may also include improving the efficiency of the MPP search and using surrogate models for the original limit-state functions. Another future work can be including a lower bound, e.g., lack of fusion, in the analysis. This task requires to develop a relevant limit-state function.

As indicated in the case study, the effects of uncertainty on the feasible design regions are significant. How to reduce the effects also needs a further investigation. We can perform sensitivity analysis to identify the important input random variables that contribute most to the gap and then reduce their uncertainty accordingly. We can also perform probabilistic design to optimally change design variables so that the effects of uncertain are minimized.

Acknowledgment

The work is conducted under CCDC Army Research Laboratory Cooperative Research and Development Agreement 19-013-001. Jing Zhang acknowledges the support from the National Science Foundation under grant numbers CMMI 1832745 and CMMI 1936290. Xiaoping Du would like to acknowledge the support from the National Science Foundation under grant number CMMI 1924413.

Conflict of Interest

There are no conflicts of interest.

Data Availability Statement

The datasets generated and supporting the findings of this article are obtained from the corresponding author upon reasonable request. The authors attest that all data for this study are included in the paper.

References

[1] Zhang, J., and Jung, Y.-G., 2018, *Additive Manufacturing: Materials, Processes, Quantifications and Applications*, Butterworth-Heinemann, Oxford, UK.

[2] Zhang, Y., Wu, L., Guo, X., Kane, S., Deng, Y., Jung, Y. G., Lee, J. H., and Zhang, J., 2017, "Additive Manufacturing of Metallic Materials: A Review," J. Mater. Eng. Perform., **17**, pp. 1–13.

[3] King, W. E., Barth, H. D., Castillo, V. M., Gallegos, G. F., Gibbs, J. W., Hahn, D. E., Kamath, C., and Rubenchik, A. M., 2014, "Observation of Keyhole-Mode Laser Melting in Laser Powder-Bed Fusion Additive Manufacturing," J. Mater. Process. Technol., **214**(12), pp. 2915–2925.

[4] Yadroitsev, I., Krakhmalev, P., Yadroitsava, I., Johansson, S., and Smurov, I., 2013, "Energy Input Effect on Morphology and Microstructure of Selective Laser Melting Single Track From Metallic Powder," J. Mater. Process. Technol., **213**(4), pp. 606–613.

[5] Guo, Q., Zhao, C., Escano, L. I., Young, Z., Xiong, L., Fezzaa, K., Everhart, W., Brown, B., Sun, T., and Chen, L., 2018, "Transient Dynamics of Powder Spattering in Laser Powder Bed Fusion Additive Manufacturing Process Revealed by In-Situ High-Speed High-Energy X-Ray Imaging," Acta Mater., **151**, pp. 169–180.

[6] Parab, N. D., Zhao, C., Cunningham, R., Escano, L. I., Fezzaa, K., Everhart, W., Rollett, A. D., Chen, L., Sun, T., Parab, N. D., Zhao, C., Cunningham, R., Escano, L. I., Fezzaa, K., Everhart, W., Rollett, A. D., Chen, L., and Sun, T., 2018, "Ultrafast X-Ray Imaging of Laser–Metal Additive Manufacturing Processes," J. Synchrotron Radiat., **25**(5), pp. 1467–1477.

[7] Caggiano, A., Zhang, J., Alfieri, V., Caiazzo, F., Gao, R., and Teti, R., 2019, "Machine Learning-Based Image Processing for On-Line Defect Recognition in Additive Manufacturing," CIRP Ann., **68**(1), pp. 451–454.

[8] Jafari-Marandi, R., Khanzadeh, M., Tian, W., Smith, B., and Bian, L., 2019, "From In-Situ Monitoring Toward High-Throughput Process Control: Cost-Driven Decision-Making Framework for Laser-Based Additive Manufacturing," J. Manuf. Syst., **51**, pp. 29–41.

[9] Ye, D., Hong, G. S., Zhang, Y., Zhu, K., and Fuh, J. Y. H., 2018, "Defect Detection in Selective Laser Melting Technology by Acoustic Signals With Deep Belief Networks," Int. J. Adv. Manuf. Technol., **96**(5–8), pp. 2791–2801.

[10] Verma, A., Tyagi, S., and Yang, K., 2015, "Modeling and Optimization of Direct Metal Laser Sintering Process," Int. J. Adv. Manuf. Technol., **77**(5–8), pp. 847–860.

[11] Zhang, J., Wu, L., Zhang, Y., and Meng, L., 2019, "Phase Field Simulation of Dendritic Microstructure in Additively Manufactured Titanium Alloy," Met. Powder Rep., **74**(1), pp. 20–24.

[12] Zhang, Y., Xiao, X., and Zhang, J., 2019, "Kinetic Monte Carlo Simulation of Sintering Behavior of Additively Manufactured Stainless Steel Powder Particles Using Reconstructed Microstructures From Synchrotron X-Ray Microtomography," Results Phys., **13**, p. 102336.

[13] Zhang, Y., and Zhang, J., 2019, "Modeling of Solidification Microstructure Evolution in Laser Powder Bed Fusion Fabricated 316L Stainless Steel Using Combined Computational Fluid Dynamics and Cellular Automata," Addit. Manuf., **28**, pp. 750–765.

[14] Khairallah, S. A., Anderson, A. T., Rubenchik, A., and King, W. E., 2016, "Laser Powder-Bed Fusion Additive Manufacturing: Physics of Complex Melt Flow and Formation Mechanisms of Pores, Spatter, and Denudation Zones," Acta Mater., **108**, pp. 36–45.

[15] Zhang, Y., Jung, Y.-G., and Zhang, J., 2020, "Chapter One—Multiscale and Multiphysics Modeling of Metal AM," *Multiscale Modeling of Additively Manufactured Metals*, Y. Zhang, Y.-G. Jung, and J. Zhang, ed., Elsevier, New York, pp. 1–10.

[16] Francis, J., and Bian, L., 2019, "Deep Learning for Distortion Prediction in Laser-Based Additive Manufacturing Using Big Data," Manuf. Lett., **20**, pp. 10–14.

[17] Meng, L., and Zhang, J., 2020, "Process Design of Laser Powder Bed Fusion of Stainless Steel Using a Gaussian Process-Based Machine Learning Model," JOM, **72**(1), pp. 420–428.

[18] Tapia, G., Khairallah, S., Matthews, M., King, W. E., and Elwany, A., 2018, "Gaussian Process-Based Surrogate Modeling Framework for Process Planning in Laser Powder-Bed Fusion Additive Manufacturing of 316L Stainless Steel," Int. J. Adv. Manuf. Technol., **94**(9–12), pp. 3591–3603.

[19] Tapia, G., King, W., Johnson, L., Arroyave, R., Karaman, I., and Elwany, A., 2018, "Uncertainty Propagation Analysis of Computational Models in Laser Powder Bed Fusion Additive Manufacturing Using Polynomial Chaos Expansions," ASME J. Manuf. Sci. Eng., **140**(12), p. 121006.

[20] Hu, Z., and Mahadevan, S., 2017, "Uncertainty Quantification and Management in Additive Manufacturing: Current Status, Needs, and Opportunities," Int. J. Adv. Manuf. Technol., **93**(5–8), pp. 2855–2874.

[21] Hu, Z., and Mahadevan, S., 2017, "Uncertainty Quantification in Prediction of Material Properties During Additive Manufacturing," Scr. Mater., **135**, pp. 135–140.

[22] Lopez, F., Witherell, P., and Lane, B., 2016, "Identifying Uncertainty in Laser Powder Bed Fusion Additive Manufacturing Models," ASME J. Mech. Des., **138**(11), p. 114502.

[23] Meng, L., McWilliams, B., Jarosinski, W., Park, H.-Y., Jung, Y.-G., Lee, J., and Zhang, J., 2020, "Machine Learning in Additive Manufacturing: A Review," JOM, **72**(6), pp. 2363–2377.

[24] Gunenthiram, V., Peyre, P., Schneider, M., Dal, M., Coste, F., Koutiri, I., and Fabbro, R., 2018, "Experimental Analysis of Spatter Generation and Melt-Pool Behavior During the Powder Bed Laser Beam Melting Process," J. Mater. Process. Technol., **251**, pp. 376–386.

[25] Liu, Y., Yang, Y., Mai, S., Wang, D., and Song, C. J. M., 2015, "Investigation Into Spatter Behavior During Selective Laser Melting of AISI 316L Stainless Steel Powder," Mater. Des., **87**, pp. 797–806.

[26] Tapia, G., Elwany, A., and Sang, H., 2016, "Prediction of Porosity in Metal-Based Additive Manufacturing Using Spatial Gaussian Process Models," Addit. Manuf., **12**, pp. 282–290.

[27] Jin, S., Iquebal, A., Bukkapatnam, S., Gaynor, A., and Ding, Y., 2019, "A Gaussian Process Model-Guided Surface Polishing Process in Additive Manufacturing," ASME J. Manuf. Sci. Eng., **142**(1), p. 011003.

[28] You, S., Guan, J., Alido, J., Hwang, H. H., Yu, R., Kwe, L., Su, H., and Chen, S., 2020, "Mitigating Scattering Effects in Light-Based Three-Dimensional Printing Using Machine Learning," ASME J. Manuf. Sci. Eng., **142**(8), p. 081002.

[29] Wang, Z., Liu, P., Xiao, Y., Cui, X., Hu, Z., and Chen, L., 2019, "A Data-Driven Approach for Process Optimization of Metallic Additive Manufacturing Under Uncertainty," ASME J. Manuf. Sci. Eng., **141**(8), p. 081004.

[30] Hann, D. B., Iammi, J., and Folkes, J., 2011, "A Simple Methodology for Predicting Laser-Weld Properties From Material and Laser Parameters," J. Phys. D: Appl. Phys., **44**(44), p. 445401.

[31] Du, X., 2012, "Reliability-Based Design Optimization With Dependent Interval Variables," Int. J. Numer. Methods Eng., **91**(2), pp. 218–228.

[32] Du, X., Sudjianto, A., and Huang, B., 2005, "Reliability-Based Design With the Mixture of Random and Interval Variables," J. Mech. Des., **127**(6), pp. 1068–1076.

[33] Zhuang, X., Pan, R., and Du, X., 2015, "Enhancing Product Robustness in Reliability-Based Design Optimization," Reliab. Eng. Syst. Saf., **138**, pp. 145–153.

[34] Du, X., Chen, W., and Wang, Y., 2010, "Most Probable Point-Based Methods," Extreme Statistics in Nanoscale Memory Design, Springer, New York, pp. 179–202.

[35] Gholaminezhad, I., Assimi, H., Jamali, A., and Vajari, D. A., 2016, "Uncertainty Quantification and Robust Modeling of Selective Laser Melting Process Using Stochastic Multi-Objective Approach," Int. J. Adv. Manuf. Technol., **86**(5–8), pp. 1425–1441.

[36] Du, X., and Chen, W., 2004, "Sequential Optimization and Reliability Assessment Method for Efficient Probabilistic Design," ASME J. Mech. Des., **126**(2), pp. 225–233.

[37] Hasofer, A. M., and Lind, N. C., 1974, "Exact and Invariant Second-Moment Code Format," J. Eng. Mech. Div., **100**(1), pp. 111–121.

[38] Rosenblatt, M., 1952, "Remarks on a Multivariate Transformation," Ann. Math. Stat., **23**(3), pp. 470–472.

[39] Ma, L., Fong, J., Lane, B., Moylan, S., Filliben, J., Heckert, A., and Levine, L., 2015, "Using Design of Experiments in Finite Element Modeling to Identify Critical Variables for Laser Powder Bed Fusion," International Solid Freeform Fabrication Symposium, Austin, TX, Aug. 10–12.

[40] Badrossamay, M., and Childs, T., 2007, "Further Studies in Selective Laser Melting of Stainless and Tool Steel Powders," Int. J. Mach. Tools Manuf., **47**(5), pp. 779–784.

[41] Khairallah, S. A., and Anderson, A., 2014, "Mesoscopic Simulation Model of Selective Laser Melting of Stainless Steel Powder," J. Mater. Process. Technol., **214**(11), pp. 2627–2636.

[42] Kim, C. S., 1975, *Thermophysical Properties of Stainless Steels*, Argonne National Lab, Lemont, IL.